Interfacial Microstructure of Neutral and Charged Polymer Brushes: A Density Functional Theory Study

*Leying Qing[1], Jian Jiang[1,2, *]*

1. Beijing National Laboratory for Molecular Sciences, State Key Laboratory of Polymer Physics and Chemistry, Institute of Chemistry, Chinese Academy of Sciences, Beijing 100190, P. R. China

2. University of Chinese Academy of Sciences, Beijing 100049, P. R. China

Abstract

Polymer density functional theory (PDFT) is a computationally efficient and popular statistical mechanics theory of complex fluids for capturing the interfacial microstructure of grafted polymer brushes (PBs). Undoubtedly, the intramolecular and intermolecular interactions in PDFT (e.g., excluded volume interactions and electrostatic interactions) are affected by the grafting behaviors. However, how to treat these interactions coupled with the physical constraints of end-grafted PBs remains unclear in the literature. Even worse, there are remarkable differences in the density profiles of PBs between the predictions from PDFT and simulations. Herein, we propose a PDFT for studying neutral and charged grafted PBs, and provide its rigorous derivation and numerical details. This PDFT is successfully validated, where the density distributions of neutral and weakly charged PBs predicted by the PDFT are in excellent agreement with the results from Monte Carlo (MC) and molecular dynamics (MD) simulations. This work provides a powerful and accurate theoretical method to reveal the interfacial microstructure of grafted PBs.

KEYWORDS

Polymer brushes (PBs), Density functional theory (DFT), Monte Carlo (MC) simulation, molecular dynamics (MD) simulation.

Introduction

Polymer brushes (PBs) are assembled by anchoring polymeric chains onto a surface, triggering an increasing interest due to the unique chemical and structural characteristics of polymeric chains.[1-2] So far, PBs have made significant contributions to a broad range of traditional and emerging applications such as biological lubrication[3], thermal and electrical stimuli-responsive surface[4], colloidal stabilization and surface protection[5], novel substrate modification,[6-7] biosensing and nanomaterial synthesis, etc.[8] These applications are highly dependent on the interfacial microstructure of PBs and straightforwardly benefited from its precise tuning.[9-10] Thus, accurate density distribution of PBs on the molecular level become a focus of attention in surface modification.

The interfacial microstructure of PBs has been investigated extensively using experiments, simulations, and theories in the last decades.[11] However, the high-throughput measurements of interfacial microstructure are difficult and inefficient for experimental methods (e.g., atomic force microscopy[12]). Currently, simulations and theories have become increasingly irreplaceable for microstructure evaluation and molecular design. Despite the success and accuracy of Monte Carlo (MC) and molecular dynamics (MD) simulations, it remains challenging due to the computational cost.[13-16] For example, the charged PBs require special methods to compute the long-range Coulomb interactions, which needs long runtimes to guarantee the data reliability in the MC/MD simulations. Differently, the theoretical approach provides a low-cost alternative for the systematical study of PBs by controlling a series of key parameters such as grafting density, chain length, block features, etc. Specifically, Alexander[17] and de Gennes[18] pioneeringly proposed a simple scaling theory based on a step-function density distribution to analyze the thermodynamic properties of PBs. Later, self-consistent field theory was adopted to study PBs,[19] and presented a

parabolic density distribution under specific conditions.[20] In recent years, Lian et al.[21] captured the parabolic-like density distribution of PBs with the help of lattice density functional theory (DFT). At the same time, they mentioned that there is a clear difference in the interfacial density profiles between lattice DFT and simulations. Undoubtedly, consistent predictions between theories and simulations are required to assert the reliability and accuracy of theoretical methods.[22-24]

Polymer DFT (PDFT) is a well-established statistical mechanical theory for complex fluids, in which the polymer chains in fluids are modeled as tangentially jointed hard spheres with considering excluded-volume interactions and electrostatic interactions, etc.[25-26] Successfully, the density profile predictions of polymers in fluids from PDFT agree well with the simulation results.[27-29] Yet, the application of PDFT in grafted PBs is not apparent owing to the physical constrains from the grafting behaviors. In other words, the limited accessible space of grafted PBs greatly alters the translational and conformational entropies of the untethered polymer chain in the vicinity of the surface. In the last few decades, PDFT has been used to study grafted PBs.[30-37] However, the significant deviations in the interfacial density distributions between PDFT and simulations are found in the literature.[38] The accurate and reliable predictions of PDFT leave much to be desired in the relevant thermodynamic and structural properties (e.g., the capacitance of supercapacitors).

In this work, we revisit the application of PDFT in the end-grafted PB systems. Firstly, a rigorous derivation of PDFT coupled with the physical constraints of end-grafted PBs is provided. Then, the equilibrium density profiles of neutral and charged end-grafted PBs from MC and MD simulations are introduced to calibrate the PDFT predictions. We find the excellent agreement between PDFT and MC/MD simulations for the neutral and weakly charged PBs, demonstrating the reliability of PDFT. And a little deviation is captured within the cases with strongly charged

PBs, which may be due to the difference in model between PDFT and MD simulations and the increasing contribution of ion-ion electrostatic correlations.

The remainder of this work is organized as follows. Firstly, molecular model and theory are given, including three different grafted PBs, rigorous derivation of PDFT, theoretical numerical details, and MD simulation implementations. Next, the comparisons of neutral and charged PBs between PDFT and MC/MD simulations are presented. Finally, the main points are summarized.

Molecular Model and Theory

Molecular Model

A flexible sequence-defined polymer chain is modeled as freely-jointed tangential hard spheres, composed of N_p blocks, where the mth block of a polymer chain has N_p^m monomers. Therefore, the total number of monomers in a polymer chain is equal to $\mathcal{N}_\mathrm{p} = \sum_{m=1}^{m=N_\mathrm{p}} N_\mathrm{p}^m$, also known as the polymerization of chain. Here, the diameter and valency of each monomer i are denoted by σ_i and Z_i, respectively. Moreover, the monomers in a block have identical features. Thus, the diameters and valence of monomers in the mth block are denoted by σ_p^m and Z_p^m, respectively. In this work, we set that the first block is formed by a neutral monomer, i.e., $N_\mathrm{p}^1 = 1$ and $Z_\mathrm{p}^1 = 0$ ($Z_1 = 0$), and the remaining blocks have different features. **Figure 1 (a)** displays three representative neutral and charged polymer chains. For **Case I**, the neutral chain has two blocks (i.e., $N_\mathrm{p} = 2$), where the second block consists of multiple neutral monomers (e.g., $N_\mathrm{p}^2 > 1$ and $Z_\mathrm{p}^2 = 0$). For **Case II**, the partially charged polymer chain is assembled from alternating neutral and charged monomers, in which the charged monomer carries a single unit of negative charge, $Z_i e$, where $Z_i = -1$ and e is the elementary charge. For **Case III**, the fully charged polymer with two blocks is

considered, in which the valency of all monomers in the second block is $Z_p^2 = -1$. As shown in the

right inset of **Figure 1 (a)**, the end-grafted PBs are formed by anchoring the first neutral monomers

of M chains to a flat structureless hard wall along the z direction. If the surface area of hard wall

is S, the grafting density of the end-grafted PBs is $\rho_g = M / S$.

Figure 1 (b)-(d) show three well-assembled PBs: neutral PB (**Case I**), partially charged PB

(**Case II**) and fully charged PB (**Case III**). For the charged PBs, the counterions with diameter σ_c

and valency $Z_c = +1$ are added to ensure the electroneutrality of system. Its number is determined

by the net charges of PBs and the charges loaded on surface (i.e., surface charge density Q_s). Note

that the subscripts p and c represent polymer chain and counterions, respectively. In this work,

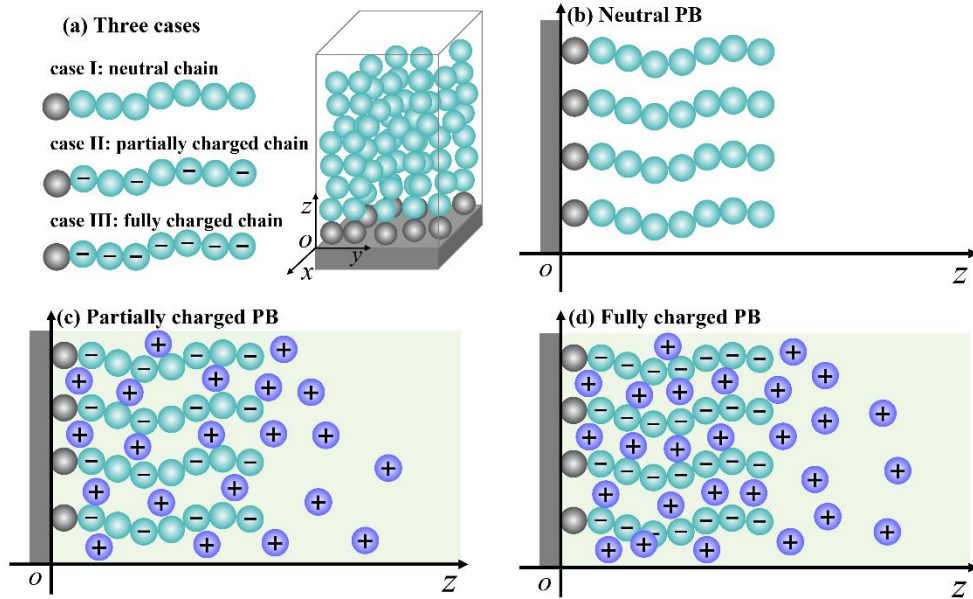the diameters of all particles are $\sigma = 0.4$ nm, i.e., $\sigma_p^m = \sigma_i = \sigma_c = \sigma$.

Figure 1. Schematic representation of the simulative PBs anchored on the hard wall at $z = 0$. (a)

three representative cases; (b) neutral PB; (c) partially charged PB; (d) fully charged PB.

In our model, two adjacent monomers in a polymer chain are tightly connected by the bonding potential $V_p^b(\mathbf{R})$, i.e.,

$$\exp\left[-\beta V_p^b(\mathbf{R})\right] = a^{\mathcal{N}_p - 1} \prod_{i=1}^{\mathcal{N}_p - 1} \frac{\delta\left(\left|\mathbf{r}_p^{i+1} - \mathbf{r}_p^i\right| - d_p^{i,i+1}\right)}{4\pi\left(d_p^{i,i+1}\right)^2} \tag{1}$$

where $\beta = 1/k_B T$ with Boltzmann constant k_B and temperature T. $\mathbf{R} \equiv \left(\mathbf{r}_p^1, \cdots, \mathbf{r}_p^{\mathcal{N}_p}\right)$ presents the spatial coordinates of all monomers in a polymer chain. The normalization parameter a can be specified as the cube of thermal de Broglie length, and its precise value has no thermodynamic consequences. $d_p^{i,i+1}$ is the bond length between two tangentially adjacent monomers. Thus, it has $d_p^{i,i+1} = \left(\sigma_p^m + \sigma_p^{m+1}\right)/2$ at the junction of the mth block and the $(m+1)^{\text{th}}$ block, otherwise $d_p^{i,i+1} = \sigma_p^m$. Apparently, Eq. (1) is essentially the bonding potential of an ideal flexible chain (i.e., random-walk or freely-jointed chain).[27]

The external interaction between hard wall and particle i is described via hard-wall potential,

$$V_{\text{ext}}^i(z) = \begin{cases} \infty, & z \leq \sigma_i/2 \\ 0, & z > \sigma_i/2 \end{cases} \tag{2}$$

where z is the distance from the hard wall; and $i \in \left[1, \cdots, \mathcal{N}_p, \mathcal{N}_p + 1\right]$, in which $i = 1, \cdots, \mathcal{N}_p$ is the monomers in a polymer chain and $i = \mathcal{N}_p + 1$ specifically refers to the counterions. It is worth to note that there is no counterion for neutral PB systems. Thus, i only belongs to $\left[1, \cdots, \mathcal{N}_p\right]$.

Here, we define $\rho_p^i(z)$ as the one-dimensional density profile of monomer i along the z direction perpendicular to the surface. Since one end of the grafted chain is anchored at $z = 0.5\sigma_1$, the physical constraint of grafted PBs is

$$\rho_p^1(z) = \rho_g \delta\left(z - \frac{\sigma_1}{2}\right) \tag{3}$$

where $\rho_p^1(z)$ is the density distribution of the grafted monomer, and σ_1 is the diameter of the grafted monomer. δ is the Dirac-delta function. In addition, another physical constraint of grafted PBs is that the accessible stretching space is limited by the chain length. Thus, the density profile of the remaining monomers satisfies,

$$\int_{\sigma_i/2}^{l_i} \rho_p^i(z)dz = \rho_g, \quad i = 2,3,\cdots,\mathcal{N}_p \tag{4}$$

where $l_i = l_{i-1} + d_p^{i,i-1}$ with $l_1 = \sigma_1/2$, representing the maximum stretching distance of the ith monomer in the grafted PBs.

According to the physical constraints of grafted PBs, the theoretical calculations of PDFT are carried out in NVT ensemble, i.e., particle number N, system volume V, temperature T are fixed. Even for charged PBs, the counterions tend to surround the charged monomers via electrostatic interactions. Therefore, NVT ensemble is reasonable when all counterions and monomers are encapsulated in a sufficiently large box.

Polymer Density Functional Theory

In the presence of an external potential, the free energy of the system $\mathcal{G}_{brush}$ is expressed as

$$\mathcal{G}_{brush} = \mathcal{F} + \int d\mathbf{R}\rho_p(\mathbf{R})V_{ext}^p(\mathbf{R}) + \ln\left(\frac{1}{\tilde{P}}\right)\int d\mathbf{r}\rho_p(\mathbf{R}) + \int d\mathbf{r}\rho_c(\mathbf{r})V_{ext}^c(\mathbf{r}) + \ln\left(\frac{1}{\tilde{C}}\right)\int d\mathbf{r}\rho_c(\mathbf{r}) \tag{5}$$

where $\tilde{P}$ and $\tilde{C}$ are the self-consistent parameters determined by the physical constraints of the grafted polymer chain and counterions, respectively. $\rho_c(\mathbf{r})$ is the density profiles of counterions and $\rho_p(\mathbf{R})$ is the density profiles of entire polymer chain. The relation between $\rho_p(\mathbf{R})$ and $\rho_p^i(\mathbf{r})$ follows

$$\rho_p^i(\mathbf{r}) = \int d\mathbf{R}\,\delta(\mathbf{r} - \mathbf{r}_p^i)\rho_p(\mathbf{R}). \tag{6}$$

Typically, Helmholtz free energy $\mathcal{F}$ in Eq. (5) is divided into two parts: the ideal gas contribution $\mathcal{F}_{id}$ and the excess term due to the intramolecular/intermolecular interactions $\mathcal{F}_{ex}$. The former is well-known as

$$\beta\mathcal{F}_{id} = \int d\mathbf{R}\rho_p(\mathbf{R})\left\{\ln[\rho_p(\mathbf{R})\Lambda_p] - 1\right\} + \int d\mathbf{r}\rho_c(\mathbf{r})\left\{\ln[\rho_c(\mathbf{r})a_c] - 1\right\}$$
$$+ \int d\mathbf{R}\rho_p(\mathbf{R})\beta V_p^b(\mathbf{R}) \tag{7}$$

where $\Lambda_p = a_p^{\mathcal{N}_p}$. a_p and a_c are volume scales of monomer and counterion respectively, set to $a_p = a_c = a$. By minimizing $\mathcal{G}_{brush}$ with respect to density profiles under the physical constraints of grafted PBs (i.e., Eq. (3) and Eq. (4)), we can obtain the Euler-Lagrange equations,

$$\rho_p(\mathbf{R})a_p^{\mathcal{N}_p} = \tilde{P}\exp\left\{-\beta V_p^b(\mathbf{R}) - \beta\sum_{i=1}^{\mathcal{N}_p}\left[\frac{\delta\mathcal{F}_{ex}}{\delta\rho_p^i(\mathbf{r})} + V_{ext}^i(\mathbf{r})\right]\right\}$$
$$= \tilde{P}\exp\left\{-\beta V_p^b(\mathbf{R}) - \beta\sum_{i=1}^{\mathcal{N}_p}\lambda_p^i(\mathbf{r})\right\} \tag{8}$$

$$\rho_c(\mathbf{r})a_c = \tilde{C}\exp\left\{-\beta\left[\frac{\delta\mathcal{F}_{ex}}{\delta\rho_c(\mathbf{r})} + V_{ext}^c(\mathbf{r})\right]\right\} = \tilde{C}\exp\left\{-\beta\lambda_c(\mathbf{r})\right\} \tag{9}$$

where $\lambda_p^i(\mathbf{r})$ and $\lambda_c(\mathbf{r})$ are the local chemical potential of the ith monomer in a polymer chain and the counterions, respectively. $\lambda_p^i(\mathbf{r})$ and $\lambda_c(\mathbf{r})$ can be understood as the effective energy field in the presence of an external potential. According to Eq. (6), the density profile of the ith monomer in a polymer chain $\rho_p^i(\mathbf{r})$ is

$$\rho_p^i(\mathbf{r})a_p = \tilde{P}\int d\mathbf{R}\,\delta(\mathbf{r} - \mathbf{r}_p^i)\exp\left\{-\beta V_p^b(\mathbf{R}) - \beta\sum_{i=1}^{\mathcal{N}_p}\lambda_p^i(\mathbf{r})\right\} \tag{10}$$

Incorporating with the bonding potential shown in Eq. (1), Eq. (10) is rewritten as

$$\rho_p^i(\mathbf{r})a_p = \tilde{P}\exp\left[-\beta\lambda_p^i(\mathbf{r})\right]G_L^i(\mathbf{r})G_R^i(\mathbf{r}) \tag{11}$$

9

where $G_L^i(\mathbf{r})$ and $G_R^i(\mathbf{r})$ are left and right propagators of the ith monomer in a polymer chain, which is determined by the recurrence relation. Consequently, coupled with the local energy field (i.e., $\lambda_p^i(\mathbf{r})$ and $\lambda_c(\mathbf{r})$) and the propagators (i.e., $G_L^i(\mathbf{r})$ and $G_R^i(\mathbf{r})$), the density profiles of monomers and counterions can be obtained with the help of the self-consistent parameters (i.e., $\tilde{P}$ and $\tilde{C}$). In this work, only one-dimensional density profiles of monomers and counterions along the z direction will be calculated, i.e., $\rho_p^i(z)$ and $\rho_c(z)$, owing to the translational invariance in the x and y directions. Next, the rigorous derivation of the local energy field and propagators for grafted PBs will be presented.

I. Excess Helmholtz Free Energy

In this work, the excess Helmholtz free energy in neutral PBs is $\mathscr{F}_{ex} = \mathscr{F}_{hs}$ and that in charged PBs includes two terms, $\mathscr{F}_{ex} = \mathscr{F}_{hs} + \mathscr{F}_C$. Specifically, $\mathscr{F}_{hs}$ describes the excess contributions from hard-core interactions including the excluded volume effect from hard-sphere fluid $\mathscr{F}_{hs}^o$ and the non-bonded chain connectivity $\mathscr{F}_{hs}^{ch}$. The former can be computed through the modified fundamental measure theory (MFMT).[39-40] $\mathscr{F}_{hs}^{ch}$ can be calculated through the first-order perturbation theory (TPT1).[29, 41] $\mathscr{F}_C$ stands for the direct Coulomb interactions.

A. Excess Free Energy from Hard-Core Interactions

The excess Helmholtz free energy due to the excluded volume effect from hard-sphere fluid is given by

$$\mathscr{F}_{hs}^o\left[\{\rho_i(\mathbf{r})\}\right] = \int d\mathbf{r}\, \phi_{hs}^o\left[\{n_k(\mathbf{r})\}\right], \quad i = 1, \ldots, \mathscr{N}_p, \mathscr{N}_p + 1 \tag{12}$$

10

where $\rho_i(\mathbf{r}) = \rho_p^i(\mathbf{r})$ for $i = 1, \ldots, \mathcal{N}_p$ and $\rho_{\mathcal{N}_p+1}(\mathbf{r}) = \rho_c(\mathbf{r})$. $\phi_{hs}^o\left[\{n_k(\mathbf{r})\}\right]$ is the excess free energy density dependent on six weighted densities, i.e., n_0, n_1, n_2, n_3, $\mathbf{n}_{V_1}$ and $\mathbf{n}_{V_2}$. Each weighted density is calculated by $n_k(\mathbf{r}) = \sum_{i=1}^{\mathcal{N}_p+1} n_k^i(\mathbf{r})$, where $n_k^i(\mathbf{r})$ is the weighted density of particle i. According to the MFMT, the excess free energy density reads

$$\phi_{hs}^o\left[\{n_k(\mathbf{r})\}\right] = -n_0 \ln(1-n_3) + \frac{n_1 n_2 - \mathbf{n}_{V_1}\mathbf{n}_{V_2}}{1-n_3} + \frac{n_2^3 - 3n_2\mathbf{n}_{V_2}\mathbf{n}_{V_2}}{36\pi}\left[\frac{\ln(1-n_3)}{n_3^2} + \frac{1}{n_3(1-n_3)^2}\right] \quad (13)$$

The excess Helmholtz free energy due to the non-bonded chain connectivity $\mathcal{F}_{hs}^{ch}$ follows

$$\mathcal{F}_{hs}^{ch}\left[\{\rho_i(\mathbf{r})\}\right] = \int d\mathbf{r}\,\phi_{hs}^{ch}\left[\{n_k(\mathbf{r})\}\right], \quad i = 1, \ldots, \mathcal{N}_p \quad (14)$$

where the excess free energy density $\phi_{hs}^{ch}\left[\{n_k(\mathbf{r})\}\right]$ is calculated by the TPT1,

$$\phi_{hs}^{ch}\left[\{n_k(\mathbf{r})\}\right] = \frac{n_0^p}{\mathcal{N}_p}\xi_p\left[\sum_{m=1}^{N_p}\left(1-N_p^m\right)\ln g_{m,m}^{hs,p} - \sum_{m=1}^{N_p-1}\ln g_{m,m+1}^{hs,p}\right] \quad (15)$$

with

$$g_{m_1,m_2}^{hs,p} = \frac{1}{1-n_3} + \frac{n_2\xi}{2(1-n_3)^2}\frac{\sigma_p^{m_1}\sigma_p^{m_2}}{\sigma_p^{m_1}+\sigma_p^{m_2}} + \frac{n_2^2\xi}{18(1-n_3)^3}\left(\frac{\sigma_p^{m_1}\sigma_p^{m_2}}{\sigma_p^{m_1}+\sigma_p^{m_2}}\right)^2 \quad (16)$$

where $\xi_p = 1 - \mathbf{n}_{V_2}^p \cdot \mathbf{n}_{V_2}^p / \left(n_2^p\right)^2$ and $\xi = 1 - \mathbf{n}_{V_2} \cdot \mathbf{n}_{V_2} / \left(n_2\right)^2$. n_0^p, n_2^p and $\mathbf{n}_{V_2}^p$ are the weighted densities of polymer chain, i.e., $n_0^p = \sum_{i=1}^{\mathcal{N}_p} n_0^i$, $n_2^p = \sum_{i=1}^{\mathcal{N}_p} n_2^i$ and $\mathbf{n}_{V_2}^p = \sum_{i=1}^{\mathcal{N}_p} \mathbf{n}_{V_2}^i$.

Apparently, the excess Helmholtz free energy from the hard-core interactions is closely associated with the weighted densities in the MFMT and TPT1. The weighted density of particle is calculated through

$$n_k^i(\mathbf{r}) = \int \rho_i(\mathbf{r}')\omega_k(\mathbf{r}-\mathbf{r}'; R_i)\,d\mathbf{r}' \quad (17)$$

where $\omega_k(\mathbf{r}-\mathbf{r}';R_i)$ is the weighted function with $k = 0, 1, 2, 3, V_1$ and V_2. The weighted functions ω_2, ω_3 and $\boldsymbol{\omega}_{V_2}$ are

$$\omega_2(\mathbf{r}-\mathbf{r}';R_i) = \delta(R_i - |\mathbf{r}-\mathbf{r}'|) \tag{18}$$

$$\omega_3(\mathbf{r}-\mathbf{r}';R_i) = \theta(R_i - |\mathbf{r}-\mathbf{r}'|) \tag{19}$$

$$\boldsymbol{\omega}_{V_2}(\mathbf{r}-\mathbf{r}';R_i) = \frac{\mathbf{r}}{|\mathbf{r}|}\delta(R_i - |\mathbf{r}-\mathbf{r}'|) \tag{20}$$

The remaining weighted functions ω_0, ω_1 and $\boldsymbol{\omega}_{V_1}$ can be obtained via

$$\omega_0(\mathbf{r}-\mathbf{r}';R_i) = \frac{\omega_2(\mathbf{r}-\mathbf{r}';R_i)}{4\pi R_i^2} \tag{21}$$

$$\omega_1(\mathbf{r}-\mathbf{r}';R_i) = \frac{\omega_2(\mathbf{r}-\mathbf{r}';R_i)}{4\pi R_i} \tag{22}$$

$$\boldsymbol{\omega}_{V_1}(\mathbf{r}-\mathbf{r}';R_i) = \frac{\boldsymbol{\omega}_{V_2}(\mathbf{r}-\mathbf{r}';R_i)}{4\pi R_i} \tag{23}$$

According to the translational invariance in the x and y directions, $n_2^i(z)$, $n_3^i(z)$, $\mathbf{n}_{V_2}^i(z)$ are derived in the cylindrical coordinate with $R_i = 0.5\sigma_i$.

$$n_2^i(z) = \pi\sigma_i\int_{z-\frac{\sigma_i}{2}}^{z+\frac{\sigma_i}{2}} \rho_i(z')dz' \tag{24}$$

$$n_3^i(z) = \pi\int_{z-\frac{\sigma_i}{2}}^{z+\frac{\sigma_i}{2}} \rho_i(z')\times\left[0.25\sigma_i^2 - (z-z')^2\right]dz' \tag{25}$$

$$\mathbf{n}_{V_2}^i(z) = 2\pi\frac{\mathbf{z}}{z}\int_{z-\frac{\sigma_i}{2}}^{z+\frac{\sigma_i}{2}} \rho_i(z')(z-z')dz' \tag{26}$$

Correspondingly, n_0^i, n_1^i, and $\mathbf{n}_{V_1}^i$ are obtained with the help of n_2^i and $\mathbf{n}_{V_2}^i$. As mentioned above, the density profile of the first monomer is fixed by the physical constraints of end-grafted PBs.

Therefore, for $i = 1$, incorporating Eq. (3) into Eqs. (24), (25), and (26), the weighted densities of the end-grafted monomer $n_2^1(z)$, $n_3^1(z)$ and $\mathbf{n}_{V_2}^1(z)$ are

$$n_2^1(z) = \pi\sigma_1 \int_{z-\frac{\sigma_1}{2}}^{z+\frac{\sigma_1}{2}} \rho_g \delta\left(z' - \frac{\sigma_1}{2}\right) dz' = \begin{cases} \pi\sigma_1\rho_g, 0 \leq z \leq \sigma_1 \\ 0 \quad , z > \sigma_1 \end{cases} \tag{27}$$

$$n_3^1(z) = \pi \int_{z-\frac{\sigma_1}{2}}^{z+\frac{\sigma_1}{2}} \rho_g \delta\left(z' - \frac{\sigma_1}{2}\right) \times \left[\frac{\sigma_1^2}{4} - (z-z')^2\right] dz' = \begin{cases} \pi\rho_g\left[\frac{\sigma_1^2}{4} - \left(z - \frac{\sigma_1}{2}\right)^2\right], 0 \leq z \leq \sigma_1 \\ 0 \quad\quad\quad , z > \sigma_1 \end{cases} \tag{28}$$

$$\mathbf{n}_{V_2}^1(z) = \frac{\mathbf{z}}{z} 2\pi \int_{z-\frac{\sigma_1}{2}}^{z+\frac{\sigma_1}{2}} \rho_g \delta\left(z' - \frac{\sigma_1}{2}\right)(z-z') dz' = \begin{cases} \frac{\mathbf{z}}{z} 2\pi\rho_g\left(z - \frac{\sigma_1}{2}\right), 0 \leq z \leq \sigma_1 \\ 0 \quad\quad , z > \sigma_1 \end{cases} \tag{29}$$

B. Direct Coulomb Interactions

The excess Helmholtz free energy due to the direct Coulomb interactions in mean field is described through a point charge model,

$$\mathcal{F}_C = \sum_{i=1}^{\mathcal{N}_p+1} Z_i e \int d\mathbf{r} \rho_i(\mathbf{r}) \psi(\mathbf{r}) - \frac{\varepsilon_0\varepsilon_r}{2} \int d\mathbf{r} \left[\nabla\psi(\mathbf{r})\right]^2 \tag{30}$$

where ε_0 is vacuum permittivity and ε_r is the relative dielectric constant. In this work, we consider an implicit aqueous solvent model, where $\varepsilon_r = 78.5$. $\psi(\mathbf{r})$ is the electrostatic potential and can be computed via Poisson equation. In one-dimensional space along the z direction, the electrostatic potential $\psi(z)$ satisfies

$$\nabla^2\psi(z) = -\frac{e}{\varepsilon_0\varepsilon_r}\left[\sum_{i=2}^{\mathcal{N}_p+1} Z_i\rho_i(z) + Z_1\rho_g\delta\left(z - \frac{\sigma_1}{2}\right)\right] \tag{31}$$

According to the boundary condition, i.e., $\psi(\infty) = 0$ and $-\frac{d\psi(z)}{dz}\bigg|_{z=0} = \frac{Q_s}{\varepsilon_0\varepsilon_r}$, the electrostatic potential of grafted PBs is derived.

For $z < \dfrac{\sigma_1}{2}$

$$\psi(z) = \frac{e}{\varepsilon_0 \varepsilon_r} \int_0^L (L-z') \sum_{i=2}^{\mathcal{N}_p+1} Z_i \rho_i(z') dz' - \frac{e}{\varepsilon_0 \varepsilon_r} \int_0^z (z-z') \sum_{i=2}^{\mathcal{N}_p+1} Z_i \rho_i(z') dz'$$
$$+ \frac{Q_s}{\varepsilon_0 \varepsilon_r}(L-z) + \frac{e}{\varepsilon_0 \varepsilon_r} Z_1 \rho_g \left(L - \frac{\sigma_1}{2}\right)$$

(32)

For $z \geq \dfrac{\sigma_1}{2}$

$$\psi(z) = \frac{e}{\varepsilon_0 \varepsilon_r} \int_0^L (L-z') \sum_{i=2}^{\mathcal{N}_p+1} Z_i \rho_i(z') dz' - \frac{e}{\varepsilon_0 \varepsilon_r} \int_0^z (z-z') \sum_{i=2}^{\mathcal{N}_p+1} Z_i \rho_i(z') dz'$$
$$+ \frac{Q_s}{\varepsilon_0 \varepsilon_r}(L-z) + \frac{e}{\varepsilon_0 \varepsilon_r} Z_1 \rho_g (L-z)$$

(33)

where L stands for the distance from the surface along the z direction, which must be sufficiently

large to ensure that all of the counterions are encapsulated in the system. In this work, we set Z_1

$= 0$, $Q_s = 0$ and $L = 80$ nm, the electrostatic potential is then computed through

$$\psi(z) = \frac{e}{\varepsilon_0 \varepsilon_r} \int_0^L (L-z') \sum_{i=2}^{\mathcal{N}_p+1} Z_i \rho_i(z') dz' - \frac{e}{\varepsilon_0 \varepsilon_r} \int_0^z (z-z') \sum_{i=2}^{\mathcal{N}_p+1} Z_i \rho_i(z') dz' \qquad (34)$$

II. Propagators

Left and right propagators of the ith monomer in a polymer chain (i.e., $G_L^i(\mathbf{r})$ and $G_R^i(\mathbf{r})$)

satisfies the recurrence relation, i.e.,

$$G_L^i(\mathbf{r}_p^i) = \begin{cases} 1 & , i = 1 \\ \int d\mathbf{r}_p^{i-1} \dfrac{\delta\left[\left|\mathbf{r}_p^i - \mathbf{r}_p^{i-1}\right| - d_p^{i,i-1}\right]}{4\pi \left(d_p^{i,i-1}\right)^2} \exp\left[-\beta \lambda_p^{i-1}\left(\mathbf{r}_p^{i-1}\right)\right] G_L^{i-1}\left(\mathbf{r}_p^{i-1}\right), & i > 1 \end{cases}$$

(35)

$$G_R^i\left(\mathbf{r}_p^i\right) = \begin{cases} \int d\mathbf{r}_p^{i+1} \dfrac{\delta\left[\left|\mathbf{r}_p^{i+1} - \mathbf{r}_p^i\right| - d_p^{i,i+1}\right]}{4\pi\left(d_p^{i,i+1}\right)^2} \exp\left[-\beta\lambda_p^{i+1}\left(\mathbf{r}_p^{i+1}\right)\right] G_R^{i+1}\left(\mathbf{r}_p^{i+1}\right), & i < \mathcal{N}_p \\ 1 & , i = \mathcal{N}_p \end{cases} \tag{36}$$

When polymer chains are tethered to hard wall, the left propagator is specified due to the fixed density profiles of the grafted monomer, see Eq. (3). For example, $G_L^2\left(\mathbf{r}_p^2\right)$ is

$$G_L^2\left(\mathbf{r}_p^2\right) = \int d\mathbf{r}_p^1 \frac{\delta\left[\left|\mathbf{r}_p^2 - \mathbf{r}_p^1\right| - d_p^{2,1}\right]}{4\pi\left(d_p^{2,1}\right)^2} \exp\left[-\beta\lambda_p^1\left(\mathbf{r}_p^1\right)\right] \times G_L^1\left(\mathbf{r}_p^1\right) \tag{37}$$

According to the translational invariance in the x and y directions, $G_L^2(z)$ is derived in the cylindrical coordinate,

$$G_L^2(z) = \frac{1}{2d_p^{2,1}} \int_{z-d_p^{2,1}}^{z+d_p^{2,1}} \exp\left[-\beta\lambda_p^1(z)\right] dz \tag{38}$$

In this work, $d_p^{2,1} = \sigma$. Then, Eq. (38) is normalized to

$$G_L^2(z) = \int_{z-\sigma}^{z+\sigma} \rho_p^1(z) dz = \int_{z-\sigma}^{z+\sigma} \rho_g \delta\left(z - \frac{\sigma}{2}\right) dz = \begin{cases} \rho_g, & 0 \le z \le 1.5\sigma \\ 0, & \text{otherwise} \end{cases} \tag{39}$$

Theoretical Numerical Iteration

In accordance with the above introduction, we get a clear understanding of end-grafted PBs, i.e., the interfacial properties including the microstructures and excess free energies of grafted PBs are significantly influenced by the physical constraints of the grafted monomer. In the theoretical numerical implementations of grafted PBs, the density profiles of monomers and counterions are set to be step-function density distributions in the first iterative step (i.e., $t = 1$) according to the physical constraints of grafted PBs. Then, the new density profiles at the next iterative step are

calculated with the help of two key self-consistent determined parameters (i.e., $\tilde{P}$ and $\tilde{C}$). The numerical details are introduced as follows.

I. Initial Density Profiles

The density profiles of monomers and counterions in the tth iterative step are defined as $\rho_{\text{p},t}^i(z)$ and $\rho_{\text{c},t}(z)$, respectively, which are initialized through grafting density, chain length, and charge amount. According to the physical constraint given by Eq. (4), the initial density profile of the ith monomer in a polymer chain, $\rho_{\text{p},t=1}^i(z)\left(i = 2, \cdots, \mathcal{N}_{\text{p}} \right)$, is calculated via

$$\rho_{\text{p},t=1}^i(z) = \begin{cases} \rho_{\text{g}} / \Delta l_i, & \sigma_i / 2 \leq z \leq l_i \\ 0 & , z < \sigma_i / 2 \text{ and } z > l_i \end{cases} \tag{40}$$

where $\Delta l_i = l_i - \sigma_i / 2$, in which l_i is the accessible space of the ith monomer in a polymer chain along the z direction.

Based on the electroneutrality of system, the initial density profile of counterions is

$$\rho_{\text{c},t=1}(z) = -\frac{Q_{\text{s}}}{Z_{\text{c}}(L - \sigma/2)} - \frac{Z_1}{Z_{\text{c}}} \frac{\rho_{\text{g}}}{L - \sigma/2} - \sum_{i=2}^{\mathcal{N}_{\text{p}}} \frac{Z_i}{Z_{\text{c}}} \rho_{\text{p},t=1}^i(z) \tag{41}$$

where the three terms on the right-hand side of Eq. (41) stand for the counterions from the opposite charges loaded on the surface, the grafted monomer, and the remaining monomers in a polymer chain, respectively. It is worth to note that we only consider salt-free cases in this work. In fact, Eq. (41) is rewritten as $\rho_{\text{c},t=1}(z) = -\sum_{i=2}^{\mathcal{N}_{\text{p}}} \frac{Z_i}{Z_{\text{c}}} \rho_{\text{p},t=1}^i(z)$ owing to $Z_1 = 0$ and $Q_{\text{s}} = 0$.

II. Numerical Iteration Process

In the iteration process of the PDFT, Eqs. (8)-(11) are solved numerically under the physical constraints of grafted PBs and counterions. Firstly, the initial density profiles of monomers and

counterions, $\rho^i_{\mathrm{p},t=1}(z)$ and $\rho_{\mathrm{c},t=1}(z)$ are required as input, and the effective energy fields of

monomers and counterions (i.e., $\lambda^i_{\mathrm{p}}(z)$ and $\lambda_{\mathrm{c}}(z)$) and the propagators of polymer chain (i.e.,

$G^i_{\mathrm{L}}(z)$ and $G^i_{\mathrm{R}}(z)$) are calculated via the initial densities. Secondly, the temporary density

profiles of monomers and counterions at the second step are obtained

$$
\begin{cases}
\hat{\rho}_{\mathrm{c},t=2}(z)a_{\mathrm{c}} = \tilde{C}\exp\{-\beta\lambda_{\mathrm{c}}(z)\} \\
\hat{\rho}^i_{\mathrm{p},t=2}(z)a_{\mathrm{p}} = \tilde{P}\exp\left[-\beta\lambda^i_{\mathrm{p}}(z)\right]G^i_{\mathrm{L}}(z)G^i_{\mathrm{R}}(z)
\end{cases}
\tag{42}
$$

where the self-consistent determined parameters $\tilde{P}$ and $\tilde{C}$ can be calculated through the

following two equalities:

$$
\int_{\sigma_i/2}^{l_i}\hat{\rho}^i_{\mathrm{p},t=2}(z)dz = \rho_{\mathrm{g}}, i = 2,3,\cdots,\mathcal{N}_{\mathrm{p}}
\tag{43}
$$

and

$$
-\int_0^L Z_{\mathrm{c}}\hat{\rho}_{\mathrm{c},t=2}(z)dz = Q_{\mathrm{brush}} + Q_{\mathrm{s}}
\tag{44}
$$

where Q_{brush} is the charge storage of grafted PBs, i.e.,

$$
Q_{\mathrm{brush}} = \int_0^L \sum_{i=2}^{\mathcal{N}_{\mathrm{p}}} Z_i\hat{\rho}^i_{\mathrm{p},t=2}(z)dz + Z_1\rho_{\mathrm{g}}
\tag{45}
$$

Finally, the new density profiles of monomers and counterions at second iterative step is updated

by the following mixing rule,

$$
\begin{cases}
\rho^i_{\mathrm{p},t=2}(z) = \alpha\hat{\rho}^i_{\mathrm{p},t=2}(z) + (1-\alpha)\rho^i_{\mathrm{p},t=1}(z) \\
\rho_{\mathrm{c},t=2}(z) = \alpha\hat{\rho}_{\mathrm{c},t=2}(z) + (1-\alpha)\rho_{\mathrm{c},t=1}(z)
\end{cases}
\tag{46}
$$

where α is a mixing parameter in the Picard iteration. In the new iterative step, the density profiles

$\rho^i_{\mathrm{p},t=2}(z)$ and $\rho_{\mathrm{c},t=2}(z)$ are used as input. This iterative loop is repeated until the iterative process

converges to the equilibrium state where the difference between t and $(t+1)$ iterative steps in the

density profiles is less than an error tolerance η. In this work, $\alpha = 0.01$ and $\eta = 1 \times 10^{-7}$.

Molecular Dynamics Simulations

MD simulations are implemented to verify the accuracy of PDFT by comparing their equilibrium

density profiles of monomers and counterions. The MD simulations are performed using

LAMMPS package with Lennard-Jones (LJ) units, e.g., the reduced distance $z^* = z / \sigma$; the

reduced temperature $T^* = k_B T / \varepsilon$ with energy parameter ε.

LAMMPS package provides many pairwise interaction potentials to capture the

intramolecular/intermolecular interactions. To model the hard-core interactions, shifted Lennard-

Jones (LJ) potential u_{ij} is used to impose a purely repulsive interaction between two particles, i.e.,

$$u_{ij} = \begin{cases} 4\varepsilon_{ij} \left[\left(\dfrac{\sigma_{ij}}{r_{ij}} \right)^{12} - \left(\dfrac{\sigma_{ij}}{r_{ij}} \right)^{6} + C \right], & r_{ij} < r_{cut} \\ 0 & , r_{ij} \geq r_{cut} \end{cases} \tag{47}$$

where $\varepsilon_{ij} = \sqrt{\varepsilon_i \varepsilon_j}$ is the energy parameter; and σ_{ij} is the effective size, equal to $\sigma_{ij} = (\sigma_i + \sigma_j)/2$

. r_{cut} is the cutoff distance and C is a constant to make $u_{ij} = 0.0$ at its cutoff. To simulate the hard

sphere model, $\varepsilon_{ij} = 100 k_B T$ and $r_{cut} = \sigma$ ($C = 0.0$) are used in MD simulations. Although the

cutoff distance in this work can cause discontinuity of the force at r_{cut}, this discontinuity point has

little influence on the simulation results in LAMMPS. Therefore, it is widely used to simulate

systems with polyelectrolyte chains in the presence of counterions.[42-46]

Furthermore, the harmonic bonded potential with a sufficiently large energy parameter $K =$

$2000 k_B T$ is utilized to assemble two freely jointed hard sphere,

$$u_{\text{bond}} = K\left(r - r_{\text{b}}\right)^2 \tag{48}$$

where r_{b} is the stretching bond length, equal to $r_{\text{b}} = d_{\text{p}}^{i+1,i}$.

Besides, due to lack of the hard wall potential $V_{\text{ext}}^i(z)$ (see Eq. (2)) in LAMMPS package, we construct a strongly repulsive wall potential by using a LJ potential u_{w}^i with large energy parameter $\varepsilon_{\text{w}} = 100\,k_B T$, i.e.,

$$u_{\text{w}}^i(z) = \begin{cases} 4\varepsilon_w\left[\left(\dfrac{\sigma_i}{z+0.5\sigma_i}\right)^{12} - \left(\dfrac{\sigma_i}{z+0.5\sigma_i}\right)^6\right], & z < 0.5\sigma_i \\ 0 & , z \geq 0.5\sigma_i \end{cases} \tag{49}$$

Additionally, the Coulomb interactions are calculated using particle-particle-particle mesh (PPPM) method.[47] That is, the Coulomb pair interactions are divided into short-range and long-range contributions. Within short cutoff distance $r < r_{\text{cut}}$, the Coulomb potential is directly computed,

$$u_{\text{C}} = \chi\frac{q_i q_j}{\varepsilon_{\text{r}} r} \tag{50}$$

where χ is an energy-conversion constant. ε_{r} is relative dielectric constant of implicit solvent (e.g., $\varepsilon_{\text{r}} = 78.5$ for mimicking the aqueous solution). q_i (or q_j) is the charge of particle and normalized by $q_i^* = q_i / \sqrt{4\pi\varepsilon_0\sigma_i\varepsilon} = \pm 11.84$ with $\sigma_i = \sigma = 4.0 \times 10^{-10}$ m and $\varepsilon = k_B T = 4.1154 \times 10^{-21}$ J (or $\dfrac{\text{kg}\cdot\text{m}^2}{\text{s}^2}$). The Bjerrum length is $l_{\text{B}} = e^2 / \left(4\pi\varepsilon_0\varepsilon_{\text{r}}k_{\text{B}}T\right) = 7.144$ Å (i.e., $l_{\text{B}} = 1.786\sigma$). In this work, we set $r_{\text{cut}} = 10\sigma$. Beyond the short-range cutoff distance, PPPM method is used to compute the long-range Coulomb pairwise interactions in reciprocal space with a maximum relative error of 10^{-5}. Accounting for the non-periodic property from hard wall in the z direction,

the migration of particles is confined within a periodic unit cell of slab geometry. Typically, the periodic unit cell is set as 3.

Corresponding to the numerical calculations of the PDFT, NVT ensemble is kept by combining the Langevin dynamics integrator (its damping factor of approximately 0.001) with a constant NVE time integration. The fixed reduced temperature $T^* = k_B T / \varepsilon = 1$ with $T = 298$ K and energy parameter $\varepsilon = 4.1154 \times 10^{-21}$ J. Because polymer chains are tethered to the surface placed in the x-y plane, the periodic boundary condition is employed in the x and y directions in a three-dimensional simulation box. In the z direction, the non-periodic and fixed boundary condition is considered. Additionally, a sufficiently long relaxation time is required to reach the equilibrium state of MD simulations. Therefore, the total running time steps of simulations are larger than 1.0 $\times 10^9$ with a time step of 0.001.

Results and Discussion

The important interest of this work is to calibrate the PDFT by comparing the density profiles of monomers and counterions with the ones from MC and MD simulations. Corresponding to the three cases presented in **Figure 1**, the PDFT is used to capture the interfacial microstructure of neutral and charged PBs with different chain lengths and grafting densities.

Case I: Neutral PBs

In 2007, Borówko et al.[48] reported high-quality density profiles of neutral PBs using MC simulations, which are widely used for benchmarking in other theoretical works.[38, 49] However, there are remarkable deviations between PDFT and MC simulation, such as overestimated interfacial densities and mismatched brush heights. Here, corresponding to the four cases reported by Borówko et al., the PDFT and MD simulation are implemented to study the microstructure of neutral PBs. **Figure 2 (a)-(d)** show the density profiles of the second block in the neutral PBs with

two grafting densities (i.e., $\rho_g \sigma^2 = 0.25$ and 0.40) and two polymerizations (i.e., $\mathcal{N}_p = 4$ and 8).

For all cases, the density profiles predicted by the PDFT agree well with the results of the MC and MD simulations, providing direct evidence for the accuracy of the PDFT. Moreover, two neutral PBs with longer chain and lower grafting density are investigated by the PDFT and MD simulations, as shown in **Figure 2 (e) and (f)**. The consistent results of density profiles once again demonstrate the reliability of the PDFT.
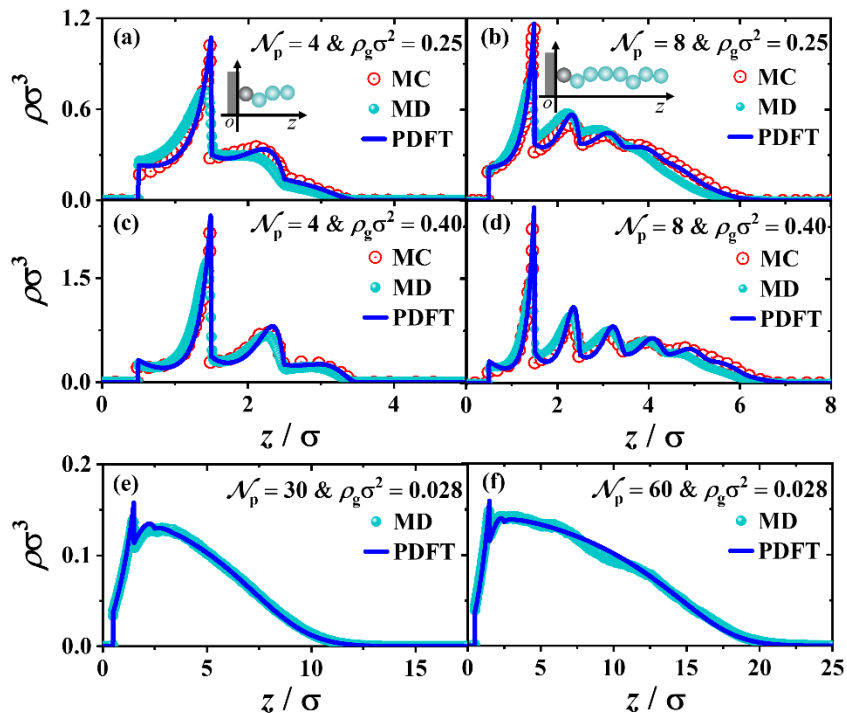
Figure 2. The density profiles of neutral PBs predicted by the PDFT and simulations: (a) $\mathcal{N}_p = 4$ and $\rho_g \sigma^2 = 0.25$; (b) $\mathcal{N}_p = 8$ and $\rho_g \sigma^2 = 0.25$; (c) $\mathcal{N}_p = 4$ and $\rho_g \sigma^2 = 0.40$; (d) $\mathcal{N}_p = 8$ and $\rho_g \sigma^2 = 0.40$; (e) $\mathcal{N}_p = 30$ and $\rho_g \sigma^2 = 0.028$; (f) $\mathcal{N}_p = 60$ and $\rho_g \sigma^2 = 0.028$. The MC data are from Ref. **48**. The MD parameters are given in **Table S1** in Supporting Information (SI)

According to **Figure 2 (d)** for the PBs with long chain and high grafting density, the density profile of the second block exhibits multiple peaks owing to the excluded volume interactions. This oscillation of density profiles weakens as the grafting density or chain length decreases, see

21

Figure 2 (a)-(c). Besides, a prominent structural feature is that the maximum peak of the density profile appears near $z = 1.5\sigma$ due to the tangential connection between the second monomer and grafted monomer. Then, along the z direction, the oscillating amplitudes of the remaining peaks decrease sequentially. After that, the density profile decreases smoothly at the outer edge of the PBs. This smoothly decreasing structure is more pronounced for the PBs with longer chain length and lower grafting density, where only a few peaks are captured in the near-interface space, see **Figure 2 (e) and (f)**.

Taking advantage of the significant spatial oscillation in the density profiles, a porous geometrical interface of PBs can be constructed to control the transport and adsorption of ions by the reversible collapse-extension transition of PBs.[50-51] In addition, the uncrowded space closest to the interface affords free small ions the opportunity to further tune the interfacial properties.

Case II: Partially Charged PBs

Like the inset in **Figure 3 (a)**, partially charged PBs are assembled from alternating neutral and charged monomers, where the first monomer grafted to the surface is neutral. Combining the excluded volume interactions and direct Coulomb interactions, the PDFT is used to study the interfacial microstructure of partially charged PBs. **Figure 3** shows the density profiles of each monomer and counterions in two partially charged PBs, i.e., (a) $\mathscr{N}_\mathrm{p} = 10$ and $\rho_\mathrm{g}\sigma^2 = 0.01$; (b) $\mathscr{N}_\mathrm{p} = 10$ and $\rho_\mathrm{g}\sigma^2 = 0.10$. When the grafting density of partially charged PBs is low, the density profiles of monomers and counterions predicted by the PDFT and MD simulation are in excellent agreement, demonstrating the validity of the PDFT.

However, when the grafting density is high, a subtle deviation between the PDFT and MD simulation is found for the monomers far from the surface. This deviation is not surprising because some approximations are introduced into the PDFT as well as the MD simulations. For example,

in the MD simulation, the shifted LJ potentials with large energy parameter and short cutoff are used to approximate the hard-wall external potential and hard-sphere interactions. Furthermore, an important factor is the increasing contribution from ion-ion electrostatic correlations. However, the ion-ion electrostatic correlations are ignored in the PDFT. Commonly, in a grand canonical ensemble, the excess Helmholtz free energy of ion-ion electrostatic correlations can be computed through a quadratic Taylor expansion with respect to a global reference density.[41, 52] However, the physical picture of this reference density is lack in this work. Thus, the ion-ion electrostatic correlations require a novel method to determine its contribution through the local densities of ions rather than a global reference density, which will be considered in our follow-up work.
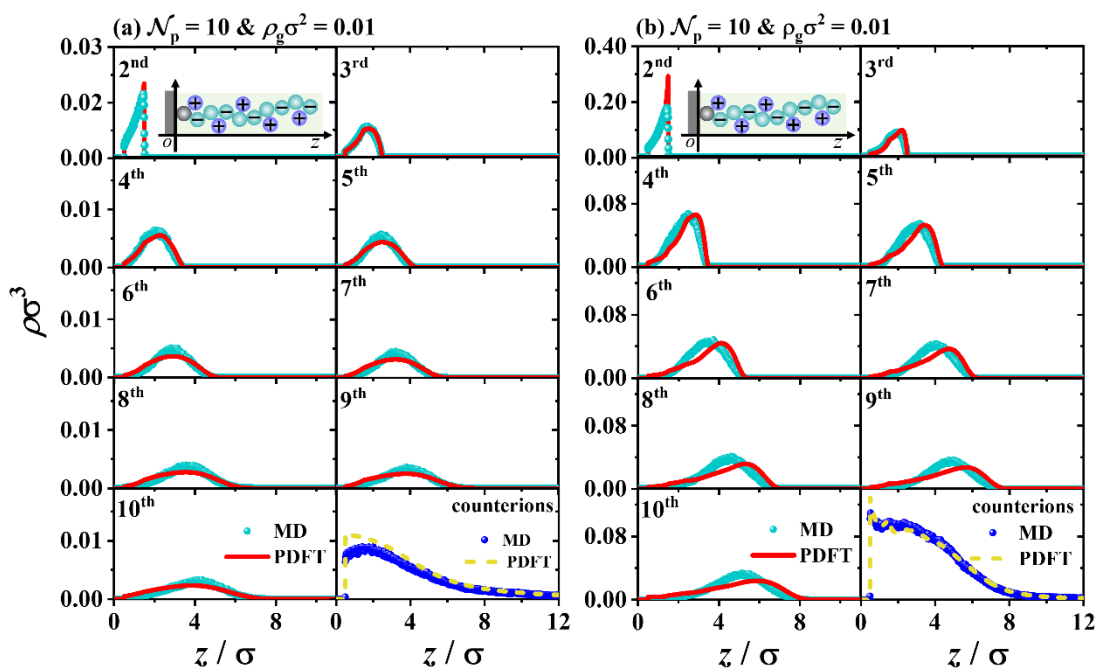

Figure 3. The density profiles of monomers and counterions predicted by the PDFT and MD simulation: (a) $\mathcal{N}_p = 10$ and $\rho_g\sigma^2 = 0.01$; (b) $\mathcal{N}_p = 10$ and $\rho_g\sigma^2 = 0.10$. Note that the 2nd represents the second monomer in a polymer chain. The MD parameters are given in **Table S2** in SI.

Similar structural characteristics are captured for those two partially charged PBs shown in **Figure 3**. A dramatic decline in the density profiles of the second monomer is observed. This sharp peak is formed because the second monomer connected to the grafted monomer is tightly confined within its maximum stretching height. Owing to the wider accessible space of the monomer farther away from the grafted monomer, we naturally capture a peak with a lower amplitude and a greater distance from the surface. Especially, the end monomers (i.e., the 10th monomer) distributes over the entire brush region, which determines the effective interfacial functional layer. As a consequence, the density profile of the monomer far from the grafted end evolves to a parabolic shape, which is different from the sharp curve of the second monomer. Additionally, though the counterions can freely move in entire space. Its density profiles show that most of counterions are concentrated within the PB layer due to the direct Coulomb interactions.

Case III: Fully Charged PBs

The fully charged PBs is assembled from two blocks, in which all of the monomers in the second block carry one elementary negative charge. Thus, the electrostatic contribution in this fully charged PBs is important. Here, three fully charged PBs are studied, i.e., $\mathcal{N}_p = 10$ and $\rho_g \sigma^2 = 0.01$; $\mathcal{N}_p = 10$ and $\rho_g \sigma^2 = 0.10$; $\mathcal{N}_p = 30$ and $\rho_g \sigma^2 = 0.028$. The PDFT and MD simulation are employed to reveal the density profiles of the second block and counterions in the fully charged PBs, as shown in **Figure 4**. Intuitively, the predictions from PDFT are well consistent with the results of MD simulations. However, there are subtle numerical differences in the density profiles on the outer edge of the fully charged PBs. Important reasons of these deviations have been mentioned above, e.g., the lack of ion-ion electrostatic correlations in the PDFT and the differences between the two models used in PDFT and MD simulation. Here, we emphasize that despite the

little differences in the density profiles of strongly charged PBs, our PDFT provides desirable

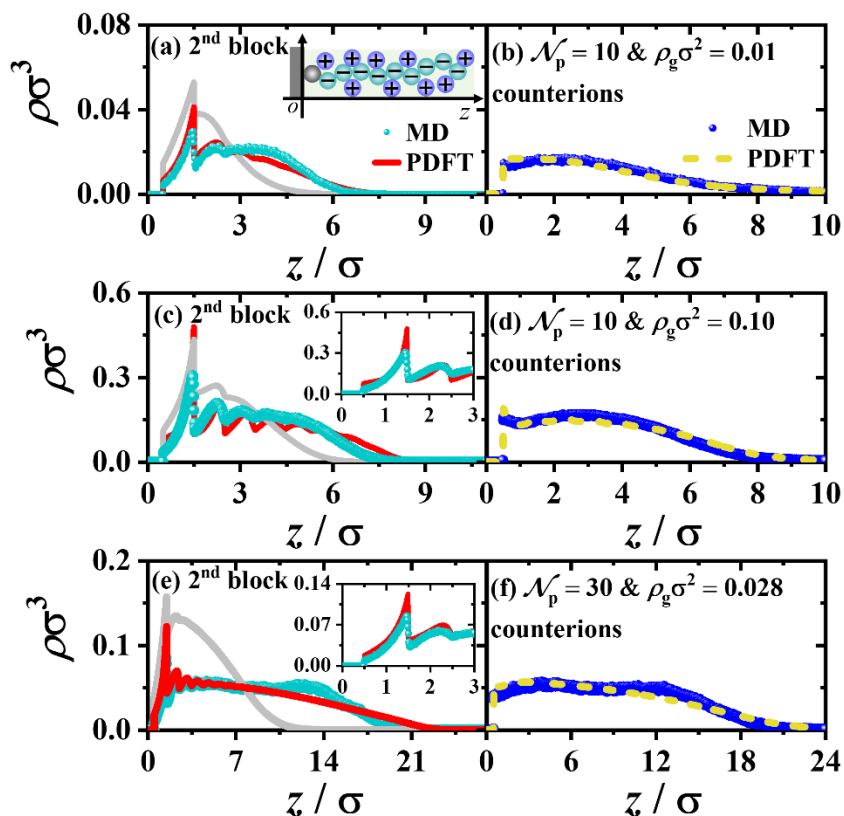accuracy and reliability in the study of interfacial microstructure of charged PBs.

Figure 4. The density profiles of the monomers in the second block (left panel) and counterions

(right panel) predicted by PDFT and MD simulation: (a)-(b) $\mathcal{N}_{\mathrm{p}} = 10$ and $\rho_{\mathrm{g}}\sigma^2 = 0.01$; (c)-(d)

$\mathcal{N}_{\mathrm{p}} = 10$ and $\rho_{\mathrm{g}}\sigma^2 = 0.10$; (e)-(f) $\mathcal{N}_{\mathrm{p}} = 30$ and $\rho_{\mathrm{g}}\sigma^2 = 0.028$. Additionally, the density profiles

of the monomers in the second block of the neutral PBs (grey solid line in the left panel) are given

for comparison, where the polymerization and grafting density of the neutral PBs are the same

with the corresponding charged PBs. The MD parameters are given in **Table S3** in SI.

Corresponding to the fully charged PBs, the neutral PBs with same polymerization and grafting

density are introduced to show the significant effect of the direct Coulomb interactions, see the

grey line in the left panel of **Figure 4**. We find that the height of charged PBs is larger than that of

neutral ones, and more peaks are observed in the charged PBs. These behaviors indicate that electrostatic interactions prefer to promote the oscillation of PBs meanwhile prolong its height, which has a positive effect on the interfacial porous energy-storage layer. In addition, when the grafting density is small, the density of charged PBs at interface is smaller than that of neutral PBs. The opposite consequence is captured for the charged PBs with large grafting density, see **Figure 4 (a) and (c)**. According to the figures in the right panel of **Figure 4**, most counterions distributes among the entire PB layer. Especially, the uncrowded space adjacent to the surface (which has been mentioned in the **Case I**) is occupied by the counterions. This finding suggests the great potential of charged PBs as the porous interfacial energy-storage layer.

4 Conclusions

In summary, a polymer density functional theory (PDFT) is rigorously extended to neutral and charged PB systems. Specifically, the hard-core interactions and direct Coulomb interactions are coupled with the physical constraints of grafted PBs. Furthermore, the PDFT is calibrated via the density profiles of the monomers and counterions provided by the MC and MD simulations. The comparison results show that the density profiles of the neutral and weakly charged PBs agree excellently with the results from MC and MD simulations, although there is a little difference between the predictions from PDFT and MD simulations in the cases with fully charged PBs. This subtle deviation may be caused by the model differences in PDFT and MD simulations as well as the lack of ion-ion electrostatic correlations in the PDFT. Altogether, beyond providing clear insight into the significant consequences of the grafting behavior, an accurate and reliable theoretical method is proposed for revealing the interfacial microstructure of neutral and charged PBs in the molecular level. We believe that this theory can be used to tune the interfacial functional layer in a reasonable way, which is benefit for many applications such as colloidal stabilization, ionic separation, and energy-storage devices.

ASSOCIATED CONTENT

Supporting Information.

The following files are available free of charge.

The parameters used in molecular dynamics (MD) simulations (PDF)

AUTHOR INFORMATION

Corresponding Author

Jian Jiang-Beijing National Laboratory for Molecular Sciences, State Key Laboratory of Polymer Physics and Chemistry, Institute of Chemistry, Chinese Academy of Sciences, Beijing 100190, P. R. China; University of Chinese Academy of Sciences, Beijing 100049, P. R. China;

ORCID: https://orcid.org/0000-0003-4171-5275; Email: jiangj@iccas.ac.cn

Author

Leying Qing- Beijing National Laboratory for Molecular Sciences, State Key Laboratory of Polymer Physics and Chemistry, Institute of Chemistry, Chinese Academy of Sciences, Beijing 100190, P. R. China;

ORCID: https://orcid.org/0000-0002-8815-1924; Email: leying@iccas.ac.cn

Notes

The authors declare no competing financial interests.

REFERENCES

(1). Milner, S. T., Polymer brushes. *Science* **1991**, *251*(4996), 905-914.

(2). Chen, W.-L.; Cordero, R.; Tran, H.; Ober, C. K., 50th anniversary perspective: Polymer brushes: Novel surfaces for future materials. *Macromolecules* **2017**, *50*(11), 4089-4113.

(3). Kreer, T., Polymer-brush lubrication: a review of recent theoretical advances. *Soft Matter* **2016**, *12*(15), 3479-3501.

(4). Sanchez-Alvarado, A. B.; Iturbe-Ek, J.; Mamidi, N.; Sustaita, A. O., Polymer brush-based thin films via Cu (0)-mediated surface-initiated atom transfer radical polymerization for sensing applications. *ACS Applied Polymer Materials* **2021**, *3*(11), 5339-5354.

(5). Wang, S.-T.; Zhang, H.; Xuan, S.; Nykypanchuk, D.; Zhang, Y.; Freychet, G.; Ocko, B. M.; Zuckermann, R. N.; Todorova, N.; Gang, O., Compact peptoid molecular brushes for nanoparticle stabilization. *Journal of the American Chemical Society* **2022**, *144*(18), 8138-8152.

(6). Ahualli, S.; Jiménez, M.; Amador, Z.; Fernández, M.; Iglesias, G.; Delgado, A., Energy production by salinity exchange in polyelectrolyte-coated electrodes. Temperature effects. *Sustainable Energy & Fuels* **2021**, *5*(13), 3321-3329.

(7). Ahualli, S.; Jimenez, M.; Fernández, M. M.; Iglesias, G.; Brogioli, D.; Delgado, A., Polyelectrolyte-coated carbons used in the generation of blue energy from salinity differences. *Physical Chemistry Chemical Physics* **2014**, *16*(46), 25241-25246.

(8). Li, D.; Xu, L.; Wang, J.; Gautrot, J. E., Responsive polymer brush design and emerging applications for nanotheranostics. *Advanced Healthcare Materials* **2021**, *10*(5), 2000953-2000971.

(9). Qing, L.; Zhao, S.; Wang, Z.-G., Surface charge density in electrical double layer capacitors with nanoscale cathode-anode separation. *The Journal of Physical Chemistry B* **2021**, *125*(2), 625-636.

(10). Qing, L.; Jiang, J., Double-edged sword of ion-size asymmetry in energy storage of supercapacitors. *Journal of Physical Chemistry Letters* **2022**, *13*(6), 1438-1445.

(11). Zoppe, J. O.; Ataman, N. C.; Mocny, P.; Wang, J.; Moraes, J.; Klok, H.-A., Surface-initiated controlled radical polymerization: state-of-the-art, opportunities, and challenges in surface and interface engineering with polymer brushes. *Chemical Reviews* **2017**, *117*(3), 1105-1318.

(12). Aktas Eken, G.; Ober, C. K., Strong polyelectrolyte brushes via alternating copolymers of styrene and maleimides: Synthesis, properties, and stability. *Macromolecules* **2022**, *55*(13), 5291-5300.

(13). Sethuraman, V.; Zheng, D.; Morse, D. C.; Dorfman, K. D., Adsorption of charge sequence-specific polydisperse polyelectrolytes. *Macromolecules* **2022**, *55*(8), 3030-3038.

(14). Sethuraman, V.; McGovern, M.; Morse, D. C.; Dorfman, K. D., Influence of charge sequence on the adsorption of polyelectrolytes to oppositely-charged polyelectrolyte brushes. *Soft Matter* **2019**, *15*(27), 5431-5442.

(15). Ahrens, H.; Förster, S.; Helm, C. A.; Kumar, N. A.; Naji, A.; Netz, R. R.; Seidel, C., Nonlinear osmotic brush regime: experiments, simulations and scaling theory. *The Journal of Physical Chemistry B* **2004**, *108*(43), 16870-16876.

(16). Murat, M.; Grest, G. S., Structure of a grafted polymer brush: A molecular dynamics simulation. *Macromolecules* **1989**, *22*(10), 4054-4059.

(17). Alexander, S., Polymer adsorption on small particles: a scaling description. *J. Phys.(Paris)* **1977**, *38*(977-983.

(18). De Gennes, P., Scaling theory of polymer adsorption. *Journal de Physique* **1976**, *37*(12), 1445-1452.

(19). Cosgrove, T.; Heath, T.; Van Lent, B.; Leermakers, F.; Scheutjens, J., Configuration of terminally attached chains at the solid/solvent interface: self-consistent field theory and a Monte Carlo model. *Macromolecules* **1987**, *20*(7), 1692-1696.

(20). Milner, S. T.; Witten, T. A.; Cates, M. E., Theory of the grafted polymer brush. *Macromolecules* **1988**, *21*(8), 2610-2619.

(21). Lian, C.; Wang, L.; Chen, X.; Han, X.; Zhao, S.; Liu, H.; Hu, Y., Modeling swelling behavior of thermoresponsive polymer brush with lattice density functional theory. *Langmuir* **2014**, *30*(14), 4040-4048.

(22). Grest, G. S.; Kremer, K.; Milner, S. T.; Witten, T., Relaxation of self-entangled many-arm star polymers. *Macromolecules* **1989**, *22*(4), 1904-1910.

(23). Chen, C.-M.; Fwu, Y.-A., Monte Carlo simulations of polymer brushes. *Physical Review E* **2000**, *63*(1), 011506-011515.

(24). Lai, P. Y.; Binder, K., Structure and dynamics of grafted polymer layers: A Monte Carlo simulation. *The Journal of Chemical Physics* **1991**, *95*(12), 9288-9299.

(25). Wu, J., Density functional theory for chemical engineering: From capillarity to soft materials. *AIChE Journal* **2006**, *52*(3), 1169-1193.

(26). Wu, J.; Li, Z., Density-functional theory for complex fluids. *Annual Review of Physical Chemistry* **2007**, *58*(1), 85-112.

(27). Jiang, J., Software package: An advanced theoretical tool for inhomogeneous fluids (Atif). *Chinese Journal of Polymer Science* **2022**, *40*(2), 220-230.

(28). Li, Z.; Wu, J., Density functional theory for planar electric double layers: closing the gap between simple and polyelectrolytes. *The Journal of Physical Chemistry B* **2006**, *110*(14), 7473-7484.

(29). Li, Z.; Wu, J., Density functional theory for polyelectrolytes near oppositely charged surfaces. *Physical Review Letters* **2006**, *96*(4), 048302-048305.

(30). Jiang, T.; Li, Z.; Wu, J., Structure and swelling of grafted polyelectrolytes: predictions from a nonlocal density functional theory. *Macromolecules* **2007**, *40*(2), 334-343.

(31). Chen, C.; Tang, P.; Qiu, F.; Shi, A.-C., Excluded volume effects in compressed polymer brushes: A density functional theory. *The Journal of Chemical Physics* **2015**, *142*(12), 124904-124913.

(32). Xu, Y.; Chen, X.; Han, X.; Xu, S.; Liu, H.; Hu, Y., Lock/unlock mechanism of solvent-responsive binary polymer brushes: Density functional theory approach. *Langmuir* **2013**, *29*(16), 4988-4997.

(33). Borówko, M.; Sokołowski, S.; Staszewski, T., Adsorption from binary solutions on the polymer-tethered surfaces. *The Journal of Physical Chemistry B* **2012**, *116*(10), 3115-3124.

(34). Jiang, T.; Wu, J., Ionic effects in collapse of polyelectrolyte brushes. *The Journal of Physical Chemistry B* **2008**, *112*(26), 7713-7720.

(35). Xu, X.; Qiu, Q.; Lu, C.; Zhao, S., Responsive properties of grafted polyanion chains: Effects of dispersion interaction and salt. *Journal of Chemical & Engineering Data* **2020**, *65*(12), 5708-5717.

(36). Jiang, T.; Wu, J., Self-organization of multivalent counterions in polyelectrolyte brushes. *The Journal of Chemical Physics* **2008**, *129*(8), 084903-084909.

(37). Ye, Y.; McCoy, J. D.; Curro, J. G., Application of density functional theory to tethered polymer chains: Effect of intermolecular attractions. *The Journal of Chemical Physics* **2003**, *119*(1), 555-564.

(38). Qiu, G.; Qiu, Q.; Qing, L.; Zhou, J.; Xu, X.; Zhao, S., Effects of Polyelectrolyte Surface Coating on the Energy Storage Performance in Supercapacitors. *The Journal of Physical Chemistry C* **2022**, *126*(19), 8218-8226.

(39). Yu, Y. X.; Wu, J., Structures of hard-sphere fluids from a modified fundamental-measure theory. *The Journal of Chemical Physics* **2002**, *117*(22), 10156-10164.

(40). Roth, R.; Evans, R.; Lang, A.; Kahl, G., Fundamental measure theory for hard-sphere mixtures revisited: The white bear version. *Journal of Physics: Condensed Matter* **2002**, *14*(46), 12063-12078.

(41). Jiang, J.; Ginzburg, V. V.; Wang, Z.-G., Density functional theory for charged fluids. *Soft Matter* **2018**, *14*(28), 5878-5887.

(42). Varghese, A.; Rajesh, R.; Vemparala, S., Aggregation of rod-like polyelectrolyte chains in the presence of monovalent counterions. *The Journal of Chemical Physics* **2012**, *137*(23), 234901-234907.

(43). Tom, A. M.; Vemparala, S.; Rajesh, R.; Brilliantov, N. V., Regimes of electrostatic collapse of a highly charged polyelectrolyte in a poor solvent. *Soft Matter* **2017**, *13*(9), 1862-1872.

(44). Tom, A. M.; Rajesh, R.; Vemparala, S., Aggregation of flexible polyelectrolytes: Phase diagram and dynamics. *The Journal of Chemical Physics* **2017**, *147*(14), 144903-144913.

(45). Tom, A. M.; Rajesh, R.; Vemparala, S., Aggregation dynamics of rigid polyelectrolytes. *The Journal of Chemical Physics* **2016**, *144*(3), 034904-034910.

(46). Allen, M.; Tildesley, D., *Computer simulation of liquids*; Oxford university press: London, 2017.

(47). Hockney, R. W.; Eastwood, J. W., *Computer simulation using particles*; CRC Press: Boca Raton, 2021.

(48). Borowko, M.; Rzysko, W.; Sokolowski, S.; Staszewski, T., Density functional approach to the adsorption of spherical molecules on a surface modified with attached short chains. *The Journal of Chemical Physics* **2007**, *126*(21), 214703-214710.

(49). Xu, X.; Cao, D., Density functional theory for adsorption of colloids on the polymer-tethered surfaces: Effect of polymer chain architecture. *The Journal of Chemical Physics* **2009**, *130*(16), 164901-164910.

(50). Adiga, S. P.; Brenner, D. W., Stimuli-responsive polymer brushes for flow control through nanopores. *Journal of Functional Biomaterials* **2012**, *3*(2), 239-256.

(51). Tagliazucchi, M.; Szleifer, I., Transport mechanisms in nanopores and nanochannels: Can we mimic nature? *Materials Today* **2015**, *18*(3), 131-142.

(52). Jiang, J.; Gillespie, D., Revisiting the charged shell model: A density functional theory for electrolytes. *Journal of Chemical Theory and Computation* **2021**, *17*(4), 2409-2416.

Microstructure of end-grafted polymer brush